# RADIATIVELY INEFFICIENT MAGNETOHYDRODYNAMIC ACCRETION-EJECTION STRUCTURES

FABIEN CASSE AND RONY KEPPENS
Foundation for Fundamental Research on Matter (FOM), Institute for Plasma Physics
Rijnhuizen, Association Euratom/FOM, P.O. Box 1207, 3430 BE Nieuwegein, Netherlands; fcasse@rijnh.nl, keppens@rijnh.nl

## ABSTRACT

We present magnetohydrodynamic simulations of a resistive accretion disk continuously launching trans-magnetosonic, collimated jets. We time-evolve the full set of magnetohydrodynamic equations but neglect radiative losses in the energetics (radiatively inefficient). Our calculations demonstrate that a jet is self-consistently produced by the interaction of an accretion disk with an open, initially bent large-scale magnetic field. A constant fraction of heated disk material is launched in the inner equipartition disk regions, leading to the formation of a hot corona and a bright collimated, superfast magnetosonic jet. We illustrate the complete dynamics of the "hot" near-steady state outflow (where thermal pressure $\simeq$ magnetic pressure) by showing force balance, energy budget, and current circuits. The evolution to this near-stationary state is analyzed in terms of the temporal variation of energy fluxes controlling the energetics of the accretion disk. We find that unlike advection-dominated accretion flow, the energy released by accretion is mainly sent into the jet rather than transformed into disk enthalpy. These magnetized, radiatively inefficient accretion-ejection structures can account for underluminous thin disks supporting bright fast collimated jets as seen in many systems displaying jets (for instance, M87).

*Subject headings:* accretion, accretion disks — galaxies: jets — ISM: jets and outflows — MHD

## 1. ACCRETION DISKS AND JETS

### 1.1. *Accretion-Ejection Models*

Astrophysical jets are quite common phenomena across our visible universe. They are typically observed in association with accreting objects such as low-mass young stellar objects (YSOs), X-ray binaries (XRBs), or active galactic nuclei (AGNs; e.g., Livio 1997 and references therein). In all these systems, the mass outflows exhibit very good collimation at large distances from the central object, as well as high velocities along the jet axis. Although operative at widely disparate length scales, these accretion-ejection systems have other features in common, in particular, observational links have been established in all cases between accretion disk luminosity and jet emission: for YSOs see, e.g., Hartigan, Edwards, & Ghandour (1995), for XRBs see Mirabel et al. (1998), and for AGNs see Serjeant et al. (1998).

The most promising unifying model relies on a scenario where an accretion disk interacts with a large-scale magnetic field in order to give birth to bipolar collimated jets (for the specific case of early protostars see also Lery, Henricksen, & Fiege 1999). Since the seminal work by Blandford & Payne (1982), it is known that the action of an open magnetic field configuration threading a disk can brake rotating matter in order to transfer angular momentum into the jet and provide energy for acceleration of jet matter. This magnetohydrodynamic (MHD) model describes the interaction of the accretion flow with a magnetic field whose origin can be due to advection of interstellar magnetic field (Mouschovias 1976) and/or dynamo produced (von Rekowski et al. 2003). The collimation of the flow is self-consistently achieved by the electric current produced by the flow itself (Heyvaerts & Norman 1989). This current provokes a radial pinching of the plasma that can balance both magnetic and thermal pressure gradients (Sauty, Trussoni, & Tsinganos 2002). The analytical

work by Blandford & Payne (1982) did make the simplifying assumption of a cold plasma.

Numerous studies have dealt with these magnetized accretion-ejection structures (MAESs) in the last two decades. Sophisticated semianalytical models deal with stationary self-similar investigations gradually extending the Blandford & Payne (1982) model with more physical effects, starting from simple vertical mass flux prescriptions (Wardle & Königl 1993) to realistic disk equilibria where ambipolar diffusion (Li 1996), resistivity (Ferreira 1997), or both viscosity and resistivity are adequately incorporated (Casse & Ferreira 2000). These studies bring deep insight in the physical conditions prevailing at the disk surface required to launch jets but fail to give realistic jet topologies in the super-Alfvénic region. The latter has spurred a variety of numerical MHD studies, aiming at a more realistic description of the trans-Alfvénic flows. The complexity of the dynamics of the accretion-ejection flow has forced many authors to either focus on jet dynamics alone (Ustyugova et al. 1995, 1999; Ouyed & Pudritz 1997; Krasnopolski, Li, & Blandford 1999) or study disk-outflow dynamics over very short timescales (Ushida & Shibata 1985; Matsumoto et al. 1996; Kato, Kudoh, & Shibata 2002). The latter class of studies were done using ideal MHD framework, which is inconsistent with long-term jet production since the frozen-in magnetic structure is advected with the disk material. This leads to a rapid destabilization of the system due to a magnetic flux accumulation in the inner part of the disk. Moreover, in most of the previous studies, the accretion disk is modeled as a non-Keplerian thick torus without any outer mass inflow that would mimic the mass reservoir of the disk outer regions. Here again this compromises the long-term jet production since accretion will end rapidly because of the lack of disk material.

In contrast to these studies, Casse & Keppens (2002, hereafter CK02) recently presented MHD computations demonstrating the launching of superfast magnetosonic,

collimated jets from a resistive accretion disk over a large number of dynamical timescales. These axisymmetric simulations heavily relied on the general requirements identified by self-similar analytical models, in particular the necessity for equipartition disk regions together with sufficiently bent magnetic surfaces (Blandford & Payne 1982; Ferriera & Pelletier 1995). Nevertheless, for simplicity CK02 replaced the energy equation by an adiabatic polytropic relation, which did not enable us to explore the energetics of the resulting accretion-ejection flow. This is of primary interest for realistic modeling, since accretion disks supporting jets display a disk luminosity much smaller than expected in the framework of any currently accepted "standard" model.

### 1.2. *Underluminous Accretion Disks and Hot Collimated Jets*

The detection of accretion-ejection motions is typically achieved through multiwavelength observations. Emissions from the disk and from an associated outflow differ since they are produced by different mechanisms in media of widely different densities and temperatures. Accretion disks displaying outflows always present low-radiative efficiency, and this is true in binary stars (Rutten, Van Paradijs, & Tinbergen 1992), microquasars (Mirabel et al. 1998), or AGNs (Di Matteo et al. 2000, 2003). One scenario to explain the lack of disk emission invokes a weak coupling between ions and electrons, resulting in electron temperatures being much lower than ion temperatures (Shapiro, Lightman, & Eardley 1976; Rees et al. 1982). This scenario has led to the concept of "advection-dominated accretion flows" (ADAFs; see, e.g., Narayan & Yi 1995 and references therein) where energy released by accretion of matter is primarily transferred to heat the ions that are ultimately advected onto the central object. If this is a black hole, this energy is then simply lost. Recently, Blandford & Begelman (1999) presented an alternative to ADAF, where inclusion of an outflow from the disk was suggested, in which case a part of the accretion energy is sent into outflowing hot matter. Although several numerical MHD simulations of radiatively inefficient accretion disks have now been reported in the literature (see Igumenshchev, Narayan, & Abramowicz 2003 and references therein), they have so far been unable to describe self-consistently both radiatively inefficient accretion flow and persistent, hot and collimated jet outflow.

The aim of the present paper is to compute radiatively inefficient magnetized accretion-ejection flow where both the inward accretion and the upward, transmagnetosonic ejection flow can provide a way out for the energy released by accretion. This is achieved by fully accounting for an appropriate energy equation in the MHD description of the interaction of an accretion disk with a large-scale magnetic field. We present the theoretical and numerical background of our model in § 2. In § 3 we display results obtained from simulations of a resistive accretion disk with full energy consideration. In § 4 we analyze the temporal evolution of the energy balance including both disk and jet powers. We conclude in § 5 with a summary and open issues to address in future work.

## 2. MAGNETIZED ACCRETION-EJECTION FLOW

We aim to model a magnetized accretion disk launching jets. The description of its plasma dynamics is achieved in an MHD framework. We first present the full set of resistive MHD equations and then discuss initial and boundary conditions. We conclude this section by explaining the physical normalization employed in our simulations, since this makes them applicable to very different systems (YSOs to AGNs).

### 2.1. *MHD Equations*

The full set of MHD equations expresses conservation of macroscopic quantities such as mass, momentum, and energy. The mass conservation is

$$\frac{\partial \rho}{\partial t} = -\nabla \cdot (\rho \boldsymbol{v}), \qquad (1)$$

where $\rho$ is the plasma density and $\boldsymbol{v}$ is the velocity of the fluid. Since we are assuming axial symmetry, note that only the poloidal component of velocity is involved in equation (1). The momentum conservation accounts for forces arising from thermal pressure $P$, Lorentz force, centrifugal force, and gravity, namely,

$$\frac{\partial \rho \boldsymbol{v}}{\partial t} + \nabla \cdot (\boldsymbol{v}\rho\boldsymbol{v} - \boldsymbol{B}\boldsymbol{B}) + \nabla\left(\frac{\boldsymbol{B}^2}{2} + \boldsymbol{P}\right) + \rho\nabla\Phi_G = 0, \quad (2)$$

where $\boldsymbol{B}$ is the magnetic field and $\Phi_G = -GM_*/(R^2 + Z^2)^{1/2}$ is the Newtonian gravity potential. Coordinates $(R, Z)$ stand for Cartesian coordinates in the poloidal plane. The temporal evolution of the magnetic field is governed by the induction equation, which must take into account the effect of a temporally and spatially varying resistivity $\eta$,

$$\frac{\partial \boldsymbol{B}}{\partial t} + \nabla \cdot (\boldsymbol{v}\boldsymbol{B} - \boldsymbol{B}\boldsymbol{v}) = -\nabla \times (\eta \boldsymbol{J}), \qquad (3)$$

where $\boldsymbol{J}$ is the current density defined by the Maxwell-Ampére equation

$$\boldsymbol{J} = \nabla \times \boldsymbol{B}. \qquad (4)$$

We have adopted units where vacuum permeability $\mu_0$ is equal to unity. The total energy density $e$ is defined as

$$e = \frac{\boldsymbol{B}^2}{2} + \frac{\rho \boldsymbol{v}^2}{2} + \frac{P}{\gamma - 1} + \rho\Phi_G, \qquad (5)$$

where $\gamma = 5/3$ is the specific heat ratio of a nonrelativistic plasma. The energy equation in a resistive framework then reads

$$\frac{\partial e}{\partial t} + \nabla \cdot \left[\boldsymbol{v}\left(e + P + \frac{\boldsymbol{B}^2}{2}\right) - \boldsymbol{B}\boldsymbol{B}\cdot\boldsymbol{v}\right] = \eta\boldsymbol{J}^2 - \boldsymbol{B}\cdot(\nabla \times \eta\boldsymbol{J}).$$
$$(6)$$

Note that resistivity, operational in the disk alone, provides a local Joule heating. Ohmically heated plasma can then be advected by both accreting and ejecting flow in the case of a radiatively inefficient plasma. The last relation closing the set of equations links pressure and density to temperature $T = P/\rho$, as we assume the plasma to be ideal.

## 2.2. *Initial Conditions*

The initial configuration of the system is very close to the one adopted in CK02. The computational domain is $[R, Z] = [0, 40] \times [0, 80]$ with a resolution of $104 \times 204$ cells and includes a sink region around the origin to avoid the gravitational singularity. The size of the sink region in CK02 was several grid cells long (up to the inner disk radius setting our unit length) and only two cells high. If one wants to simulate systems ranging from YSOs (Newtonian gravity) to black holes (with, for instance, a pseudo-Newtonian gravity [Paczynsky & Wiita 1980], suitably describing plasma dynamics from several Schwarzschild radii outward), we have to take into account the fact that the gravitational singularity does not always occur exactly at the origin but can be located at some distance from it (in the case of a black hole). Therefore, we now modify the size of the sink region and design it to cover one unit length along both $R$ and $Z$. For a complete description of the boundary conditions, for both the treatment of this interior sink region and the domain boundaries, we refer to CK02.

We briefly list our nearly unchanged initial conditions for density and velocity, namely,

$$\rho(R, Z) = \max\left[ 10^{-6}, \frac{R_0^{3/2}}{\left( R^2 + R_0^2 \right)^{3/4}} \right]$$
$$\times \left( \max\left\{ 10^{-6}, \left[ 1 - \frac{(\gamma - 1)Z^2}{2H^2} \right] \right\}^{1/(\gamma - 1)} \right),$$

$$V_R(R, Z) = -m_s \frac{R_0^{1/2}}{\left( R_0^2 + R^2 \right)^{1/4}} \exp\left( -\frac{2Z^2}{H^2} \right) = V_Z(R, Z)\frac{R}{Z},$$

$$V_\theta(R, Z) = \left( 1 - \epsilon^2 \right) \frac{R_0^{1/2}}{\epsilon \left( R_0^2 + R^2 \right)^{1/4}} \exp\left( -\frac{2Z^2}{H^2} \right). \qquad (7)$$

Note that in the present paper we have decreased the initial density range compared to CK02 for computational performance. However, we still cover six decades in density contrast at $t = 0$. Similar to CK02, we assume the initial thermal pressure to be polytropic such that $P = \rho^{5/3}$. The disk height $H = \epsilon R$ increases linearly with radius, with aspect ratio $\epsilon = 0.1$ suitable for a thin disk. The constant $R_0 = 4$, while the parameter $m_s = 0.1$ is consistent with initial subsonic accretion motion. The $m_s$ parameter range is restricted by both subsonic accretion motion and the minimal bending of the poloidal magnetic surface in order to achieve jet production (Blandford & Payne 1982). Indeed, the induction equation shows that a steady state magnetic configuration with bent magnetic surface above a thin disk requires both resistivity and minimal radial motion since

$$\eta \frac{\partial B_R}{\partial t} \sim -V_R B_Z. \qquad (8)$$

The choice of $m_s$ is then to be smaller but close to unity.

The initial magnetic field configuration is purposely taken very different from CK02. Where CK02 started from a radially stratified but purely vertical field, here we start with an open poloidal magnetic structure to address the issue of jet collimation adequately. The main difficulty is to find an ini-

tially bent magnetic configuration that reconciles several constraints like symmetry at the equatorial disk plane and at the jet axis with the obvious requirement of $\nabla \cdot \boldsymbol{B} = 0$. Moreover, if one wants to have an almost constant plasma beta $\beta_P = B^2/P \sim 1$ inside the accretion disk, a necessary condition for jet launching, the radial variation of the magnetic components must be close to a power law of index $-5/4$. In order to fulfill the above statements, we adopt the magnetic configuration ($\beta_P = 0.6$ in our simulation) that exploits the function

$$F(R, Z) = \sqrt{\beta_P} \frac{R_0^{5/4} R^2}{\left( R_0^2 + R^2 \right)^{5/8}} \frac{1}{1 + \zeta Z^2/H^2} \qquad (9)$$

and given in full by

$$B_R(R, Z) = -\frac{1}{R}\frac{\partial F}{\partial Z},$$
$$B_Z(R, Z) = \frac{1}{R}\frac{\partial F}{\partial R} + \frac{\sqrt{\beta_P}}{\left( 1 + R^2 \right)},$$
$$B_\theta(R, Z) = 0. \qquad (10)$$

The extra term appearing in the $B_Z$ definition avoids vanishing vertical magnetic field at the jet axis (this term rapidly vanishes as $R$ increases) and does not interfere with the constraint $\nabla \cdot \boldsymbol{B} = 0$. The initial magnetic field configuration is not force-free but prevents any initially induced collimation since magnetic surfaces tend to widen (outwardly decreasing magnetic pressure). In Figure 1 we have displayed this initial poloidal magnetic configuration, where we have set $\zeta = 0.04$ ($\zeta$ controlling the initial bending of magnetic surfaces).

The total energy density $e$ is then found from the previous quantities according to equation (5). The anomalous resistivity $\eta$ is prescribed in the same way as in CK02, namely,

$$\eta = \alpha_m V_A|_{Z=0} H \exp\left( -2\frac{Z^2}{H^2} \right), \qquad (11)$$

which is an $\alpha$-prescription ($\alpha_m = 0.1$) where the Alfvén velocity replaces the sonic speed (Shakura & Sunyaev 1973). Through the dependence on the Alfvén velocity, this becomes a spatiotemporally varying profile that essentially vanishes outside the disk.

## 2.3. *Numerical Code: VAC*

The numerical calculations presented here are done using the Versatile Advection Code (VAC; see Tóth 1996).[1] We solve the full set of resistive MHD equations under the assumption of a cylindrical symmetry. The initial conditions described above are time advanced using the conservative, second-order accurate Total Variation Diminishing Lax-Friedrichs (Tóth & Odstrčil 1996) scheme with minmod limiting applied on the primitive variables. We use a dimensionally unsplit, explicit predictor-corrector time marching. To enforce the solenoidal

---

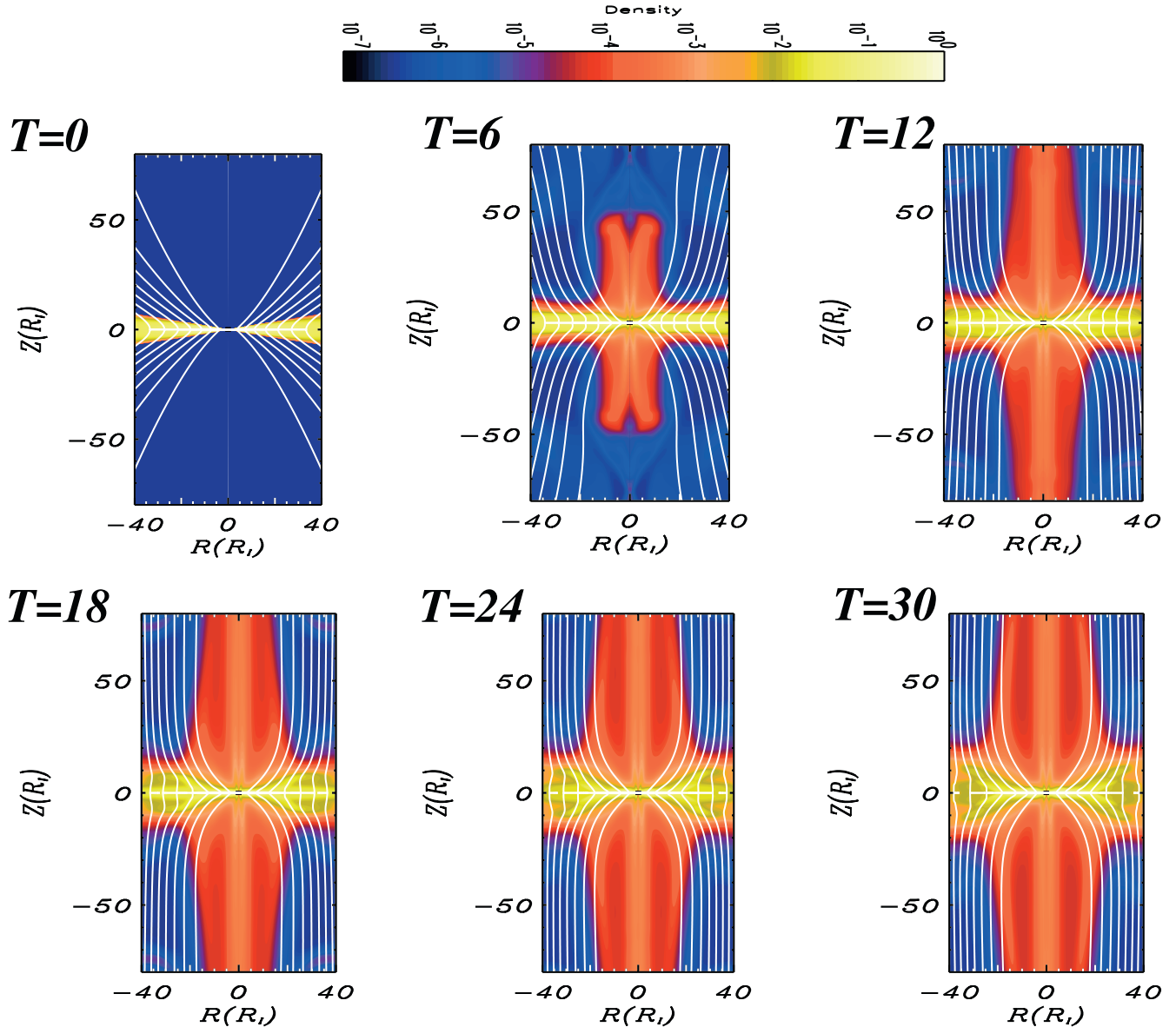[1] See also http://www.phys.uu.nl/~toth.

Fig. 1.—Temporal evolution of a resistive accretion disk threaded by a poloidal magnetic field. Color levels represent density level, while solid lines stand for poloidal magnetic field lines. The time unit labeling each snapshot is the number of rotations of the inner radius. After a few rotations, outflows are escaping from the disk and remain focused despite an initial bent poloidal magnetic configuration. Once jets are launched, the structure varies little during the remainder of the whole computation.

character of the magnetic field, we apply a projection scheme prior to every time step (Brackbill & Barnes 1980).

### 2.4. *Accretion Disk Properties*

The initial conditions discussed in § 2.2 are inspired from self-similar descriptions of accretion disks. It is important to realize that through the careful choice of normalization used in these expressions, our results will be applicable to both YSO and AGN systems. Indeed, units are now expressed in terms of inner disk radii $R = 1$, velocities from $\Omega_K H|_{R=1}$, and density values (very close to or) at $R = 1$. We here list what this dimensionalization implies for both black hole and YSO systems.

In this particular framework, the standard accretion disk model (Shakura & Sunyaev 1973; Novikov & Thorne 1973; Lynden-Bell & Pringle 1974) describes astrophysical accretion

disks provided that the accretion is sub-Eddington. If radiative pressure is neglected, it can be shown that the plasma temperature scales as

$$T_0 = \frac{\tilde{\mu} m_p \Omega_K^2 H^2}{k_B} = 10^{11} \left( \frac{R}{R_S} \right)^{-1} \text{ K},$$

$$= 10^4 \left( \frac{M_*}{M_\odot} \right) \left( \frac{R}{0.1 \text{ AU}} \right)^{-1} \text{ K}, \qquad (12)$$

where $\tilde{\mu} m_p$ is the mean molecular mass of the plasma (proton mass $m_p$), $H = \epsilon R$ is the disk height, $\Omega_K = (GM_*/R^3)^{1/2}$ is the Keplerian angular velocity, and $k_B$ is Boltzmann's constant. The first expression contains $R_S = 2GM_*/c^2$, which stands for the Schwarzschild radius, and is applicable in the case of a black hole. The second expression is to be used for a YSO disk.

This temperature scaling, combined with the definition of the accretion rate $\dot{M}_a$, leads to all other dimensional quantities. When applying our results to a certain system with inner radius $R$, central object mass $M_*$, and accretion rate $\dot{M}_a$, the dimensional scale factors are

$$V_{\theta,0} = \epsilon^{-1} V_{R,0} = \Omega_K R = 2.1 \times 10^{10} \left(\frac{R}{R_S}\right)^{-1/2} \text{ cm s}^{-1}$$

$$= 9.5 \times 10^6 \left(\frac{M_*}{M_\odot}\right)^{1/2} \left(\frac{R}{0.1 \text{ AU}}\right)^{-1/2} \text{ cm s}^{-1},$$

$$\rho_0 = \frac{\dot{M}_a}{4\pi V_{R,0} R H}$$

$$= 2.7 \times 10^5 \left(\frac{\dot{M}_a}{M_\odot \text{ yr}^{-1}}\right) \left(\frac{M_*}{M_\odot}\right)^{-2} \left(\frac{R}{R_S}\right)^{-3/2} \text{ g cm}^{-3}$$

$$= 2.4 \times 10^{-12} \left(\frac{\dot{M}_a}{10^{-7} M_\odot \text{ yr}^{-1}}\right) \left(\frac{M_*}{M_\odot}\right)^{-1/2}$$

$$\left(\frac{R}{0.1 \text{ AU}}\right)^{-3/2} \text{ g cm}^{-3},$$

$$P_0 = \rho_0 \Omega_K^2 H^2$$

$$= 1.2 \times 10^{24} \left(\frac{\dot{M}_a}{M_\odot \text{ yr}^{-1}}\right) \left(\frac{M_*}{M_\odot}\right)^{-2} \left(\frac{R}{R_S}\right)^{-5/2} \text{ ergs cm}^{-3}$$

$$= 2.1 \left(\frac{\dot{M}_a}{10^{-7} M_\odot \text{ yr}^{-1}}\right) \left(\frac{M_*}{M_\odot}\right)^{1/2} \left(\frac{R}{0.1 \text{ AU}}\right)^{-5/2} \text{ ergs cm}^{-3}. \tag{13}$$

Again, the first expressions are to be used for black hole systems, while the second lines are for YSOs.

The last quantity is the magnetic field that we set to be close to equipartition with thermal pressure, a necessary condition for jet launching. Indeed, the above temperature statement implies that thermal pressure naturally overcomes the gravitational pinching in standard accretion disk ($P \sim \rho \Omega_K^2 H^2$). Magnetized disks are also prone to magnetic pinching so a natural equilibrium of the disk is such that $P \geq B^2/\mu_0$. The former constraint, coupled with the MHD Poynting flux amplitude threshold to produce superfast magnetosonic, collimated outflows, leads to a disk configuration where $P \sim B^2/\mu_0$ (Ferreira & Pelletier 1995). The magnetic field will then be

$$B_0 = 3.9 \times 10^{12} \beta_P^{1/2} \left(\frac{\dot{M}_a}{M_\odot \text{ yr}^{-1}}\right)^{1/2} \left(\frac{M_*}{M_\odot}\right)^{-1} \left(\frac{R}{R_S}\right)^{-5/4} \text{ G}$$

$$= 7 \beta_P^{1/2} \left(\frac{\dot{M}_a}{10^{-7} M_\odot \text{ yr}^{-1}}\right)^{1/2} \left(\frac{M_*}{M_\odot}\right)^{1/4} \left(\frac{R}{0.1 \text{ AU}}\right)^{-5/4} \text{ G}. \tag{14}$$

Observations indicate that the inner parts of AGN and YSO disks mainly differ in their temperature (AGN, $\geq 10^9$ K; YSO, $\leq 10^4$ K). This difference is also evident in other properties (pressure, magnetic field), but its main consequence is that these systems have very different dominant radiative mechanisms operational, since the opacity regime varies from fully to partially ionized plasma.

## 3. ACCRETION DISKS AND "HOT" JETS

In this section we present the MHD simulations resulting from the initial configuration presented in the previous section. We first describe the temporal evolution of the accretion-ejection structure, then display the full jet launching mechanism, and finally check the radial force balance that is reached in the jet.

### 3.1. Temporal Evolution of the Flow

The result of numerically simulating the full MHD dynamics of the resistive magnetized accretion disk is displayed in Figure 1. The six snapshots represent six poloidal cross sections of the structure at different stages of its temporal evolution. The initial accretion disk configuration is close to a radial equilibrium where Keplerian rotation balances gravity of the central mass. The rotation of matter twists the initially purely poloidal magnetic field lines such that outflows appear at the surface of the disk. The outflow is continuously emitted during the further evolution of the system. As seen in the density levels of the various snapshots, this outflow is less dense $\mathcal{O}(10^{-3})$ than the accretion disk $\mathcal{O}(1)$ but denser than the surrounding medium $\mathcal{O}(10^{-6})$ by several orders of magnitude. The evolution of both the mass outflow and the magnetic field topology gets closer to an equilibrium as time increases since the poloidal velocity component of the outflow becomes parallel to the poloidal magnetic field. Moreover, the outflow is radially collimated and crosses the Alfvén and fast magnetosonic speeds, to become superfast magnetosonic well before it reaches the top boundary of the computational domain (see also CK02). It can then safely be qualified as a jet. In Figure 2 we present a three-dimensional representation of the final stationary end state reached. We visualized a magnetic surface that is anchored at $R = 3$, which nicely shows its initial fanning out, as well as its eventual collimation. Selected field lines are shown in yellow, revealing their helical character. We also plot a streamline (in blue) that shows the path of a plasma parcel that is initially accreting within the disk in a spiral fashion, until it reaches the jet launch area where it gets propelled into the jet. Finally, the figure also contains a volume rendering of the density in accretion disk-jet system, which shows that the density structure at the foot of the jet is in fact convex since full collimation is only achieved from some vertical distance above the disk. In our simulations full flow collimation occurs beyond $Z = 50$, which corresponds to typically several tens of disk scale heights.

In order to quantify the temporal evolution of both accretion and ejection flows, we can have a look at both accretion and ejection mass rates. These rates also trace the efficiency of the magnetic field to remove angular momentum from the disk (to allow accretion) and to accelerate matter in the jet (which creates a vertical mass flux as seen in Fig. 1). In Figure 3 we have displayed these mass rates as a function of time, $\dot{M}_{A,I}$ and $\dot{M}_{A,E}$ being accretion rates measured at inner radius $R_I = 1$ and external radius $R_E = 40$, respectively, while $\dot{M}_{\text{JET}} = 2\pi \int_0^{R_E} R \rho V_Z \, dR$ is the ejection mass rate measured at a given $Z$ above the disk surface. In Figure 3 the inner accretion rate is normalized with respect to the value of the outer accretion rate, which by means of our boundary conditions (fixing the mass flux) is set to be constant. The strong increase of the inner accretion rate with time is a clear translation of the role of the magnetic torque in the disk: as the simulation begins, the twist
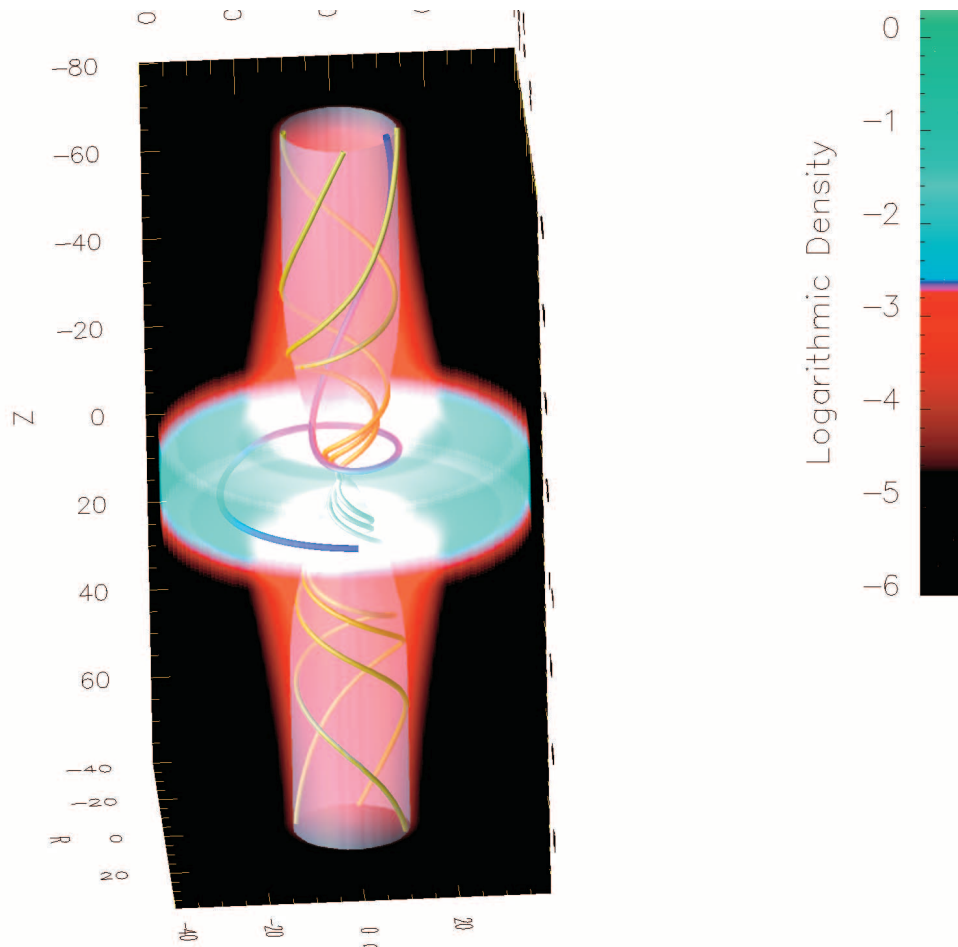
Fig. 2.—Three-dimensional impression of the final near-stationary end state reached in our simulations. Color levels represent a volume rendering of plasma density, and translucent surface stands for a magnetic surface anchored at $R = 3$ in the disk. Yellow and blue lines stand for magnetic field lines and flow streamline, respectively. As can be seen, magnetic field lines are twisted by disk rotation, which provokes mass acceleration as shown by the flow streamline that is initially accreting toward the central object and then turns into the jet.

of magnetic field lines provoked by disk rotation creates a toroidal component for the magnetic field that directly leads to a braking magnetic torque. The azimuthal braking of matter reduces the centrifugal force and thus allows matter to be attracted by gravity at a higher rate. Nevertheless, as seen in Figure 3, the increase rapidly disappears to let the inner accretion rate settle to an almost constant value. The existence of this plateau accounts for an accretion disk where matter rotation and magnetic tension reach an equilibrium state. The ejection rate is slowly rising and reaches a final value that is of the order of 22% of the inner accretion rate. During the final stages both ejection and accretion rates remain almost constant and enable us to study in detail the accretion-ejection connection. The final ratio of inner to outer accretion rates is of the order of 10. This value larger than unity arises from our choice to impose a constant outer accretion rate during the simulation, thus not enabling the structure to adjust itself to the outer part of the accretion disks that lie outside the computational domain.

Note that these accretion rates have already settled on constant values after about 10 inner orbital periods. We have evolved the system further to 30 inner orbital periods, and as seen in the snapshots from Figure 1, the overall structure remains rather stationary during that time. As the jet is confined to

within 20 inner radii, the final time $T = 30$ covers 1.3 rotation periods as measured at the external foot of the jet, or only 0.13 rotation periods of the outer radius at $R = 40$. However, as will become clear from the further analysis of the force balances achieved in the inner disk regions, this is a truly stationary configuration. Note also that because of the large density contrasts, this corresponds to several tens of thousands of CFL limited time steps, which make our simulations computationally challenging.

Note that our end state is in contrast to recent three-dimensional simulations of radiatively inefficient accretion flows (Igumenshchev et al. 2003), whose authors claim that we are focusing on a transient phase of the flow. However, the quasi-steady end state observed in Igumenshchev et al. (2003) is one of dominant magnetic field in the entire computational domain. This must be due to the imposed continuous injection of poloidal magnetic flux adopted in that study. In contrast, our simulations do not assume an infinite reservoir of magnetic flux, and the magnetic field settles into a stationary state where inward advection is balanced by outward slippage due to the disk resistivity. Moreover, in our simulation the level of magnetic pressure is always close to unity in either the accretion disk or the jet.
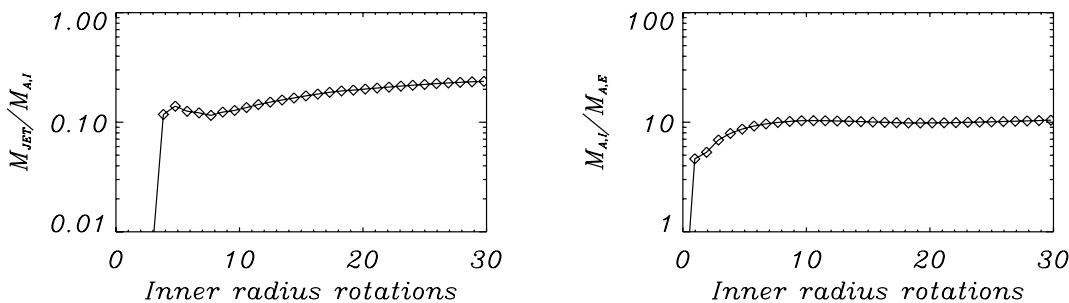
Fig. 3.—Ejection mass rates and inner accretion rates as a function of time. The inner accretion rate, normalized to the constant value of the outer accretion rate, strongly increases during the very early stages and then remains almost constant during the rest of the simulation. The ejection rate increases slowly with time and reaches a final value of the order of 20% of the inner accretion rate.

### 3.2. *Force Balance and Current Circuit*

The accretion-ejection zone, as already shown in CK02, is the most crucial area when simulating the launching of jets. A subtle balance between different forces must be obtained in order to achieve a continuous emission of matter, as well as the collimation of the resulting outflow. As an example, we display in Figure 4 the different forces in the disk equilibrium at the final time of the simulation from Figure 1. In this figure, the poloidal forces are represented along a given magnetic surface already represented in Figure 2, as well as the magnetic torque, poloidal velocity, and temperature. The vector $\hat{\boldsymbol{e}}_P$ occurring in Figure 4 is defined as $\boldsymbol{B}_P/|\boldsymbol{B}_P|$. The top left-hand panel represents the total force applied on the plasma, which is negative in the disk and becomes positive near the disk surface. As already shown in CK02, this configuration enables the matter below the disk surface to be pinched and to remain in an accretion regime, while beyond the disk surface, matter is accelerated along magnetic field lines, leading to a jet. This balance is obtained from competing forces where thermal pressure gradient and centrifugal force counteract magnetic and gravitational pinching. The crucial point of the accretion-ejection connection is to accurately capture the sign change of the sum of all forces in the numerical stationary state. This change of sign can only be achieved if the poloidal magnetic force along the magnetic surface changes its sign near the disk surface, as shown in Figure 4. Since this force is directly related to the magnetic torque,

$$(\boldsymbol{J} \times \boldsymbol{B}) \cdot \boldsymbol{B}_P = -(\boldsymbol{J} \times \boldsymbol{B}) \cdot \boldsymbol{B}_\theta, \qquad (15)$$

this also implies that the magnetic torque changes its sign there, as also shown in Figure 4. This configuration is at the core of magnetocentrifugal acceleration since toroidal acceleration (or braking) determines poloidal acceleration (or braking) of matter. The poloidal velocity field shown in Figure 4 confirms the above statements, since this field is consistent with an accretion motion in the disk (dominant negative radial velocity) while the vertical velocity becomes dominant beyond the disk surface. The angle between the poloidal velocity and poloidal magnetic field is displayed in the bottom middle panel and again confirms the required accretion-ejection configuration where flow is perpendicular to the magnetic field in the disk and becomes essentially parallel to it in the jet region.

The plasma temperature levels are displayed in the left panel of Figure 5 and exhibit an interesting behavior. In CK02, we were using a polytropic relation that was constrain-

ing the temperature to be proportional to $\rho^{\gamma-1}$. This invariably led to a jet where the temperature is very low because of the relatively low densities in the jet. As we now include the full energy equation (and include ohmic heating), this is no longer happening.

We can see in Figure 5 that the disk temperature, which was initially smaller than unity at this location, has increased, reflecting the locally operative Joule heating and gasdynamics. Rewriting energy equation (6) by subtracting momentum and induction equations leads to the temperature equation that reads

$$\frac{1}{\gamma - 1}\left(\frac{\partial T}{\partial t} + \boldsymbol{v}_p \cdot \nabla T\right) = \frac{\eta \boldsymbol{J}^2}{\rho} - T\nabla \cdot \boldsymbol{v}, \qquad (16)$$

where both ohmic heating and flow dynamics affect the behavior of the temperature. Ohmic heating is occurring inside the accretion disk and inevitably leads to a higher disk temperature than in the initial stage. In the accretion disk, the velocity divergence is negative since $\nabla \cdot \boldsymbol{v} = \partial V_Z/\partial Z + \partial V_R/\partial R + V_R/R$, where $V_R$ is a slowly radially varying negative component. This term will also account for a local heating of the plasma, even in the case where no ohmic heating would occur. Assuming the structure to be close to a steady state, one has

$$\boldsymbol{v}_p \cdot \nabla T \simeq \left(\frac{\eta \boldsymbol{J}^2}{\rho} - T\nabla \cdot \boldsymbol{v}\right)(\gamma - 1) > 0, \qquad (17)$$

which is consistent with Figure 5, where isocontours of temperature are roughly perpendicular to the streamlines in the disk. In the jet region, temperature isocontours coincide with streamlines as soon as streamlines have turned from an accretion motion ($V_R < 0$) to an ejection motion ($V_R > 0$). It is noteworthy that at this precise location we have strong negative $\nabla \cdot \boldsymbol{v}$, which leads to a sudden temperature increase. The resulting "hot" jet is a general property of this kind of outflow since it does not require local ohmic heating in the corona. We mention that performing the same simulation presented here but neglecting ohmic heating in the energy equation also gives birth to jets that have similar temperature as the disk, although slightly lower than with ohmic heating included. The relatively small influence of the ohmic heating can be explained in our case by the fact that the chosen resistivity is very low since $\eta = \alpha_m H V_A \leq 10^{-2} R$.

It is possible to clarify another aspect of the accretion-ejection mechanism by analyzing the current circuit established
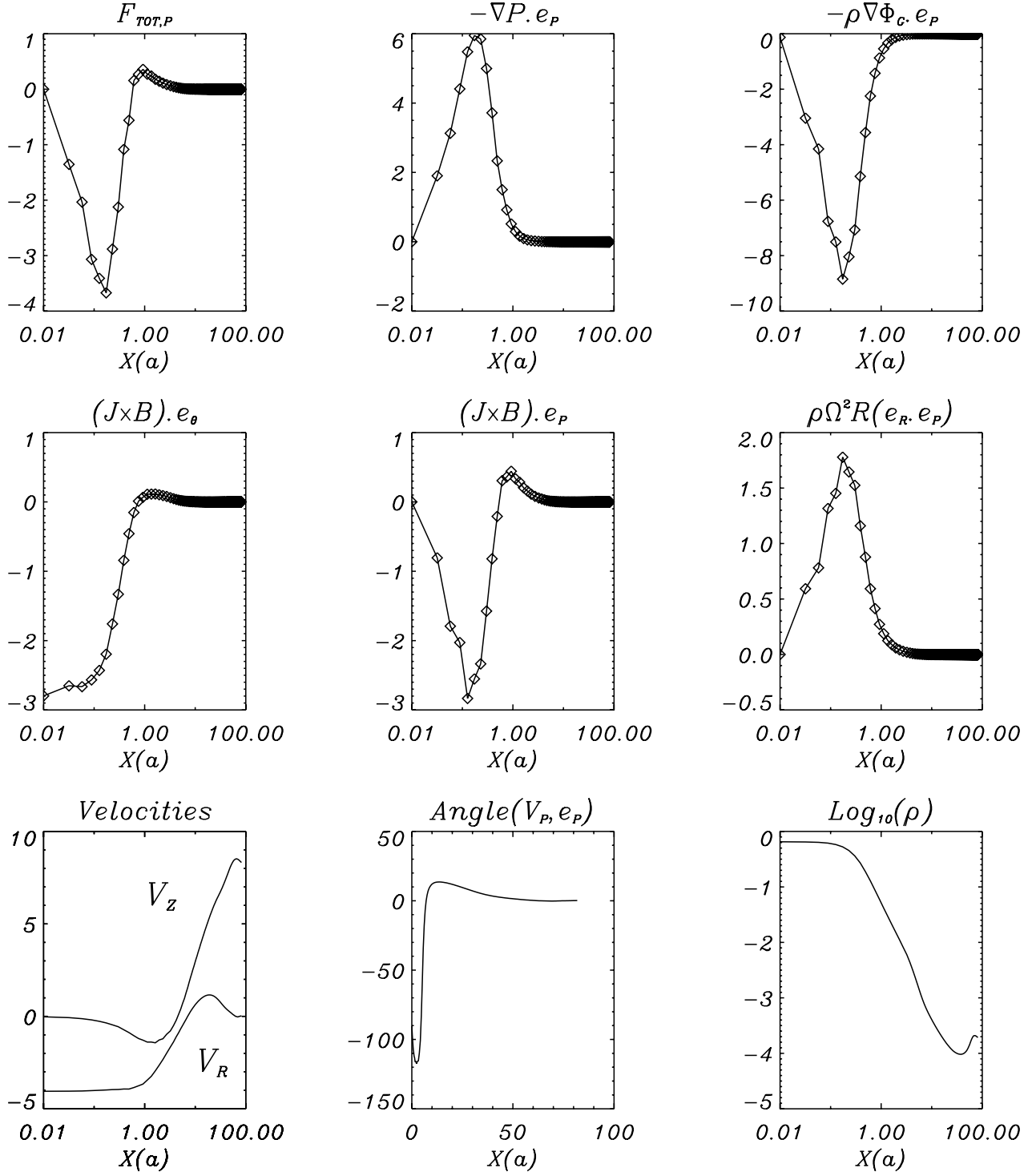
Fig. 4.—Plots of forces projected along a given magnetic surface as a function of the curvilinear abscissa along this magnetic surface $X(a)$ at $T = 30$. The footpoint of this surface is at $R = 3$. *From left to right and from top to bottom*: total force, thermal pressure gradient, gravity, magnetic torque, poloidal magnetic force, centrifugal force, radial and vertical velocities, angle between poloidal velocity, and poloidal magnetic field and density. The key to achieve an accretion-ejection configuration is to have a magnetic configuration where the Lorentz force pinches the disk and accelerates matter in the jet.

in the final structure. Indeed, in an axisymmetric framework, it is easy to calculate the current $I$ at any location thanks to the Maxwell-Ampére law stating that

$$I = \int\int \boldsymbol{J} \cdot d\boldsymbol{S} = \oint \boldsymbol{B} \cdot d\boldsymbol{l} = 2\pi R B_\theta < 0, \qquad (18)$$

where the contour in the last integral is a circle of radius $R$ with its center located at the jet axis. Rewriting the poloidal magnetic force as

$$(\boldsymbol{J} \times \boldsymbol{B}) \cdot \hat{\boldsymbol{e}}_P = -B_\theta \frac{\nabla I}{2\pi \boldsymbol{R}} \cdot \hat{\boldsymbol{e}}_P, \qquad (19)$$
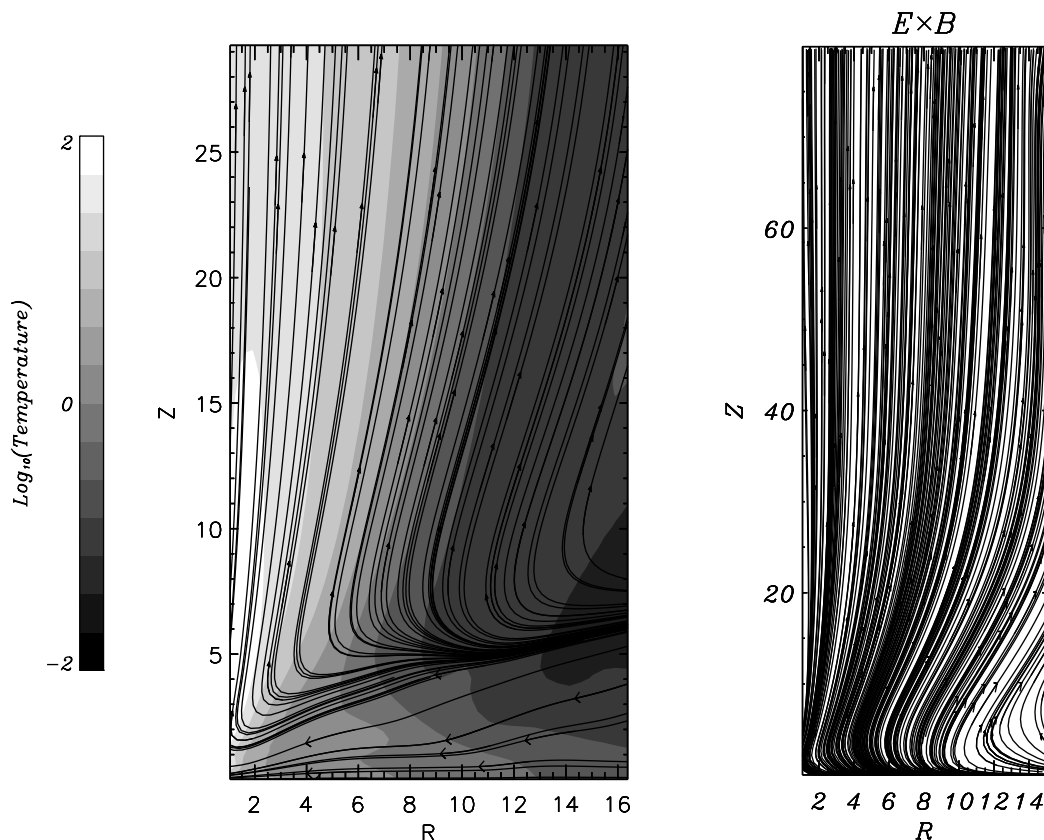
Fig. 5.—*Left*: Poloidal flow streamlines and temperature. Both accretion and ejection regimes occur. The heated plasma (ohmic heating and flow dynamics) in the disk gives birth to a "hot" jet where temperature isocontours coincide with flow streamlines. The disk aspect ratio is small thanks to a predominant energy transport achieved by jet launching rather than by enthalpy creation. *Right*: Poloidal streamlines of the MHD Poynting flux. The main part of the MHD energy flux is sent into the jet and sustains powerful hot jets.

it is clear that this force is entirely controlled by the local variation of the current along the magnetic field line. Looking back at Figure 4, where the magnetic force projected along the magnetic field line is represented, we see that the above-mentioned change of sign of the force has a direct implication for the current, namely, that the derivative of the current along the magnetic field line also changes its sign. Looking now at Figure 6, where isocontours of $I$ are displayed, we can see that this leads to the formation of closed current loops since the current $I$ start to decrease and then increase. This kind of current circuit is representative for a working accretion-ejection structure where both magnetic braking in the disk and magnetic acceleration in the jet occur. In a full meridional cross section through the disk-jet system, this is reminiscent of a "butterfly" current circuit (Ferreira 1997).

### 3.3. *Jet Collimation*

In CK02 we presented MHD simulations of accretion disks launching jets where the resulting outflow was collimated. In that work we were able to show that the radial force balance in the jet was achieved by magnetic tension counteracting magnetic pressure effects (a cold jet). Nevertheless, it was not a priori obvious that this collimation is not affected by our choice of an initial purely vertical magnetic field configuration. In the present paper we purposely choose a different initial magnetic configuration where the poloidal surfaces are strongly bent at $T = 0$ as shown in Figure 1. Still, the resulting jet is well collimated, which is a direct proof that the collimation of this flow is arising self-consistently. We

display in Figure 7 the radial balance of the jet for the same snapshot as in Figure 4 at $Z = 60$. Clearly, the total force is vanishingly small, proving that there is equilibrium in the jet, but the situation is quite different than in CK02. Indeed, now the thermal pressure is of the same order as the magnetic pressure, which leads to a qualitatively different radial jet equilibrium. The thermal pressure gradient and the centrifugal force are now balancing the total radial magnetic force. This kind of force balance between thermal pressure and magnetic force is another clue to the occurrence of a "hot" jet where thermal energy is of the same order as the magnetic energy.

In order to rule out any artificial collimation of the jet, we have performed the same simulation with different box size and boundary conditions for the magnetic field. Since Ustyugova et al. (1999), it has been shown that axisymmetric magnetic field having open boundaries may induce artificial collimation forces due to imposed vanishing radial current in the ghost cells. The authors showed that one way to obtain accurate numerical MHD flow solutions is to switch from open boundary on the toroidal magnetic field to a "force-free" one [where $\boldsymbol{B}_p \cdot \nabla(RB_\theta = 0)$] and to perform the simulation on a square domain in $R$ and $Z$. We have followed exactly the same approach as Ustyugova et al. (1999) and obtained a solution very close to the one presented in Figure 1. For instance, we present in Figure 8 the density and poloidal magnetic field structure, as well as poloidal streamlines of the flow at $T = 30$. The collimation is undoubtedly occurring since the jet magnetic and velocity fields are completely
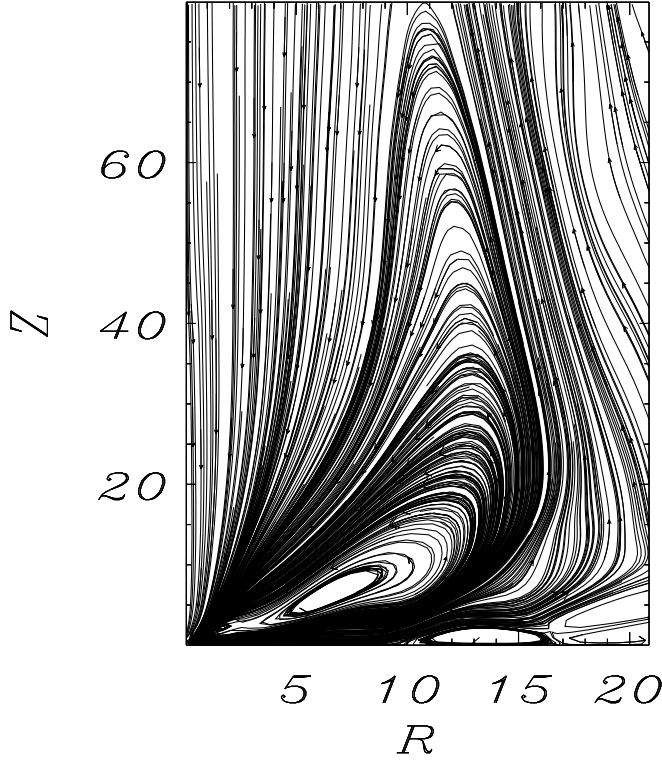
Fig. 6.—Isocontours of current $I \propto RB_\theta$. The closed current loops are direct evidence of the existence of an accretion-ejection structure where magnetic field pinches matter inside the disk and accelerates it beyond the disk surface (see § 3.2). This circuit is one "wing" of a full "butterfly" configuration.

vertical and superfast magnetosonic as the flow is escaping from the domain. The fast magnetosonic surface is shown in Figure 8 with a dot-dashed line and stands for the location where poloidal velocity equals the local fast magnetosonic velocity.

## 4. RADIATIVELY INEFFICIENT ACCRETION DISK LAUNCHING JETS

The inclusion of the energy equation in the MHD description enables us to investigate the energetics of the MAES. For instance, in classical hydrodynamical ADAF, it is shown that the energy released by accretion of matter is balanced by creation of entropy within the disk. In the present simulations, the occurrence of a dynamically significant magnetic field opens new ways to transfer and to use accretion energy. We begin this section by defining the different powers relevant for the disk energetics. Subsequently, we will analyze the temporal evolution of these quantities in order to identify the predominant way of energy transport in the flow.

### 4.1. *MHD Energy Equation*

In § 2.1 we presented the MHD equations and in particular the energy equation (6). This equation can equivalently be rewritten in a full conservative form as

$$\frac{\partial e}{\partial t} + \nabla \cdot \left[ \boldsymbol{v}\left( e + P + \frac{\boldsymbol{B}^2}{2} \right) - \boldsymbol{B}\boldsymbol{B} \cdot \boldsymbol{v} + \eta \boldsymbol{J} \times \boldsymbol{B} \right] = 0. \quad (20)$$

Using Ohm's law, we can replace the current density $\boldsymbol{J}$ by the electromotive field $\boldsymbol{E} = \boldsymbol{B} \times \boldsymbol{v} + \eta \boldsymbol{J}$ and write the general energy conservation in a form that is independent of the MHD regime (either ideal or resistive),

$$\frac{\partial e}{\partial t} + \nabla \cdot \left[ \rho \boldsymbol{v} \left( \frac{\boldsymbol{v}^2}{2} + \frac{\gamma}{\gamma - 1} \frac{\boldsymbol{P}}{\rho} + \Phi_G \right) + \boldsymbol{E} \times \boldsymbol{B} \right] = 0$$

$$\Leftrightarrow \frac{\partial e}{\partial t} + \nabla \cdot (\boldsymbol{F}_{\mathrm{acc}} + \boldsymbol{F}_{\mathrm{MHD}}) = 0. \quad (21)$$

The last term is the MHD Poynting flux. In an axisymmetric framework the two fluxes that control the temporal evolution of total energy density are as follows (only the poloidal components of these fluxes are relevant):

1. Accretion energy flux $\boldsymbol{F}_{\mathrm{acc}}$. The dominant component in the disk is the radial one since the flow components in the accretion disk obey $V_\theta \gg |V_R| \gg |V_Z|$. In standard accretion disk models (Shakura & Sunyaev 1973; Novikov & Thorne 1973; Lynden-Bell & Pringle 1974), entropy is negligible inside the disk so that this flux can be reduced to $\boldsymbol{F}_{\mathrm{acc}} \sim \rho \boldsymbol{v}_R \Phi_G / 2$. Note that in the case of a jet, the energy flux $\boldsymbol{F}_{\mathrm{acc}}$ through the disk surface can become significant.

2. MHD Poynting flux. This represents the energy carried by the magnetic field via angular momentum stored in the magnetic field. At the disk surface, where the ideal MHD regime prevails, this flux can be written as

$$\boldsymbol{F}_{\mathrm{MHD}} = \boldsymbol{v}B^2 - \boldsymbol{B}(\boldsymbol{B} \cdot \boldsymbol{v}) \simeq \boldsymbol{v}B^2 + \boldsymbol{B}|v_\theta B_\theta|, \quad (22)$$

which shows that the energy will escape from the disk along flow streamlines and magnetic field lines (which are both directed upward in the corona).

For our MHD simulations presented in the previous section, we can define and follow the evolution of the following different powers. The energy liberated by accretion is defined as

$$P_{\mathrm{LIB}} = P_{\mathrm{MEC}} + P_{\mathrm{ENT}} + P_{\mathrm{MHD}},$$

where

$$P_{\mathrm{MEC}} = -\iint_{S_I} d\boldsymbol{S}_I \cdot \rho \boldsymbol{v} \left( \frac{v^2}{2} + \Phi_G \right) - \iint_{S_E} d\boldsymbol{S}_E \cdot \rho \boldsymbol{v} \left( \frac{v^2}{2} + \Phi_G \right),$$

$$P_{\mathrm{ENT}} = -\iint_{S_I} d\boldsymbol{S}_I \cdot \rho \boldsymbol{v} \left( \frac{\gamma}{\gamma - 1} \frac{P}{\rho} \right) - \iint_{S_E} d\boldsymbol{S}_E \cdot \rho \boldsymbol{v} \left( \frac{\gamma}{\gamma - 1} \frac{P}{\rho} \right),$$

$$P_{\mathrm{MHD}} = -\iint_{S_I} d\boldsymbol{S}_I \cdot (\boldsymbol{E} \times \boldsymbol{B}) - \iint_{S_E} d\boldsymbol{S}_E \cdot (\boldsymbol{E} \times \boldsymbol{B}),$$

$$(23)$$

where the surfaces $S_I$ and $S_E$ correspond to the inner and outer vertical cut through the accretion disk ($d\boldsymbol{S}_I = -2\pi R_I \, dZ \, \hat{\boldsymbol{e}}_R$ with $-H < Z < H$ and $d\boldsymbol{S}_E = 2\pi R_E \, dZ \, \hat{\boldsymbol{e}}_R$ with $-H < Z < H$). In standard disk models, the azimuthal velocity of matter is close to Keplerian so that the energy liberated by accretion is $P_{\mathrm{LIB}} \sim GM_* \dot{M}_{A,I} / 2R_I$, where $\dot{M}_{A,I}$ is the accretion rate evaluated at the inner radius. In ADAF models, the enthalpy contribution $P_{\mathrm{ENT}}$ is not negligible, and since it is negative, the liberated energy (responsible for the disk luminosity in that particular case) is reduced. The contribution of the radial Poynting flux is more difficult to estimate inside the disk, but we will show that it is a small contribution to the liberated energy.
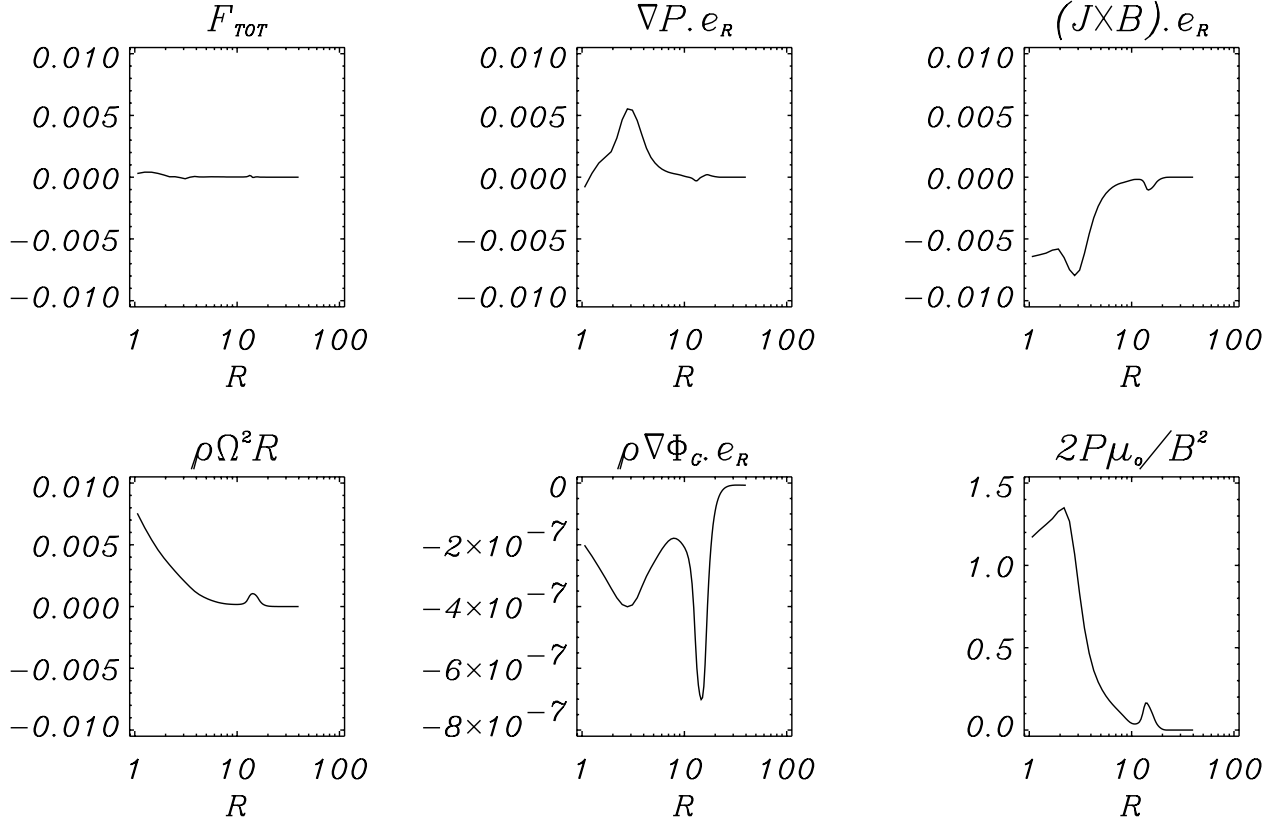
FIG. 7.—Plots of radial forces acting on the jet at $Z = 60$ and at $T = 30$. The total force is very small and ensures a good collimation for the jet. The radial equilibrium of the jet is achieved thanks to a thermal pressure gradient and centrifugal force balancing the radial magnetic force. This equilibrium where thermal pressure is of the same order as magnetic pressure is the signature of a "hot" jet.

In the present study, the occurrence of a magnetized jet outflow requires that we also evaluate the energy flux through the disk corona. Again we define a jet power $P_{\mathrm{JET}}$ such that

$$P_{\mathrm{JET}} = P_{\mathrm{MEC},J} + P_{\mathrm{ENT},J} + P_{\mathrm{MHD},J},$$

$$P_{\mathrm{MEC},J} = \int \int_{S_{\mathrm{surf}}} d\mathbf{S}_{\mathrm{surf}} \cdot \rho \mathbf{v} \left( \frac{v^2}{2} + \Phi_G \right),$$

$$P_{\mathrm{ENT},J} = \int \int_{S_{\mathrm{surf}}} d\mathbf{S}_{\mathrm{surf}} \cdot \rho \mathbf{v} \left( \frac{\gamma}{\gamma - 1} \frac{P}{\rho} \right),$$

$$P_{\mathrm{MHD},J} = \int \int_{S_{\mathrm{surf}}} d\mathbf{S}_{\mathrm{surf}} \cdot (\mathbf{E} \times \mathbf{B}), \qquad (24)$$

where $d\mathbf{S}_{\mathrm{surf}} = 2\pi R \, dR \, \hat{\mathbf{e}}_Z$ with $R_I < R < R_E$. In the disk corona, the vertical velocity of matter can be large as a result of magnetic acceleration and will produce a significant vertical energy flux. If the structure reaches a near-steady state, our energy balance would read $P_{\mathrm{MEC}} + P_{\mathrm{ENT}} + P_{\mathrm{MHD}} = P_{\mathrm{JET}}$. If neither a magnetic field nor a jet is present, this conservation gives the usual ADAF-like relation $P_{\mathrm{MEC}} \simeq -P_{\mathrm{ENT}}$ so that $P_{\mathrm{LIB}} \simeq 0$ and the disk will thus be very underluminous.

### 4.2. *Underluminous Disks Producing Jets*

We display in Figure 9 the temporal evolution of all previously defined powers that characterize the energetics of the structure. First of all, the top left-hand panel represents the temporal evolution of the energy liberated by the accretion of matter $P_{\mathrm{LIB}}$, this power being normalized to the "standard"

accretion power expected for a thin disk $P_0 = GM_* \dot{M}_{A0}/2R_I$, where $\dot{M}_{A0}$ is the inner accretion rate at $T = 0$. This power rapidly increases in early stages of the evolution and then reaches a plateau where it remains almost constant at about 10 times its standard value (mainly controlled by the inner accretion rate; see discussion in § 3.1). In the three following plots, we see the relative amplitude of each contribution to this power. The mechanical power $P_{\mathrm{MEC}}$ is the dominant contribution, while advected enthalpy $P_{\mathrm{ENT}}$ and Poynting flux $P_{\mathrm{MHD}}$ are small and of the same order, with ratios as

$$\frac{-P_{\mathrm{ENT}}}{P_{\mathrm{MEC}}} \simeq 0.27, \qquad \frac{-P_{\mathrm{MHD}}}{P_{\mathrm{MEC}}} \simeq 0.1. \qquad (25)$$

Note that these two contributions are negative, meaning that they both advect a portion of the energy through the inner radius and reduce the available disk power.

Nevertheless, these last two contributions are small compared to the mechanical energy released by accretion so that $P_{\mathrm{LIB}} \simeq 0.63 P_{\mathrm{MEC}}$. This configuration is completely different from a usual ADAF, since there one would expect to have $P_{\mathrm{LIB}} \ll P_{\mathrm{MEC}}$. The jet flow is completely responsible for this seeming discrepancy. Indeed, as shown in the bottom left-hand panel of Figure 9, the power going into the jet (evaluated at $Z = 25$) is of the same order as $P_{\mathrm{LIB}}$, which leads to an energy budget that is indeed close to a stationary state since $P_{\mathrm{LIB}} = P_{\mathrm{MEC}} + P_{\mathrm{ENT}} + P_{\mathrm{MHD}} \simeq P_{\mathrm{JET}}$. The jet power components $P_{\mathrm{MEC},J}$, $P_{\mathrm{ENT},J}$, and $P_{\mathrm{MHD},J}$ are shown in the bottom right-hand panel: the mechanical energy flux is again
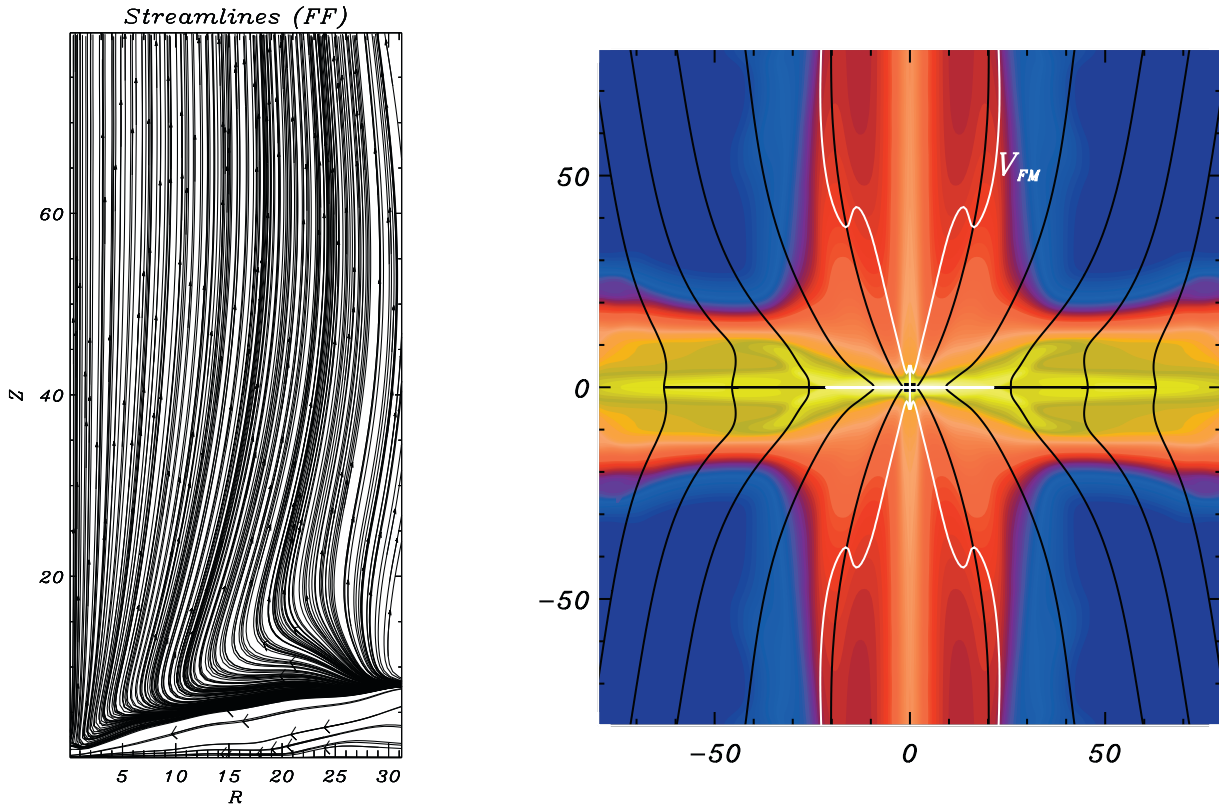
Fig. 8.—Same simulation as the last snapshot of Fig. 1, but with a square simulation domain and "force-free" boundary for the toroidal magnetic field ($J_p \times B_p = 0$). The collimation of the jet is still occurring, and the jet radius is the same as in the previous calculation. The dot-dashed line is the contour of the fast magnetosonic surface where the poloidal velocity of the flow equals the local fast magnetosonic speed.

the largest one, but other components are not negligible, in particular the jet MHD Poynting flux. This means that in the corona the magnetic field is still carrying energy and consequently that acceleration of jet matter will still occur beyond this surface located at $Z = 25$. Note also that the enthalpy flux at the base of the jet is a significant fraction of the jet power, which confirms our previous statements about the "hot" nature of the jet. As a final illustration of the energy transfer that is dominated by the jet, we show in Figure 5 both poloidal streamlines and poloidal MHD Poynting flux streamlines. We clearly see that both accretion and ejection occur and that the main part of the Poynting flux is feeding the jet structure. Moreover, the disk remains thin (as seen in the flow streamlines), although Joule heating occurs within the disk. Here again, the role of the jet is primordial since it enables the accretion disk to transfer the accretion energy into jet power rather than in disk enthalpy (temperature) that would thicken the disk.

## 5. SUMMARY AND OUTLOOK

In this paper we presented time-dependent MHD simulations of an axisymmetric, resistive accretion disk threaded by a bipolar magnetic field. The computation evolves the full set of MHD equations, including an energy equation with spatiotemporally varying resistivity triggered inside the disk only (set with an $\alpha$-type prescription). We assumed that both the viscous torque and radiative losses were negligible, so that we can deal with radiatively inefficient, magnetized accretion disks. Initial conditions were carefully designed to fulfill the requirement of jet production, i.e., starting from a near-

equipartition accretion disk. Our computations bring important new results:

1. The present simulations are the first simulations to achieve a near-stationary state consisting of a magnetized accretion disk launching trans-Alfvénic up to superfast magnetosonic, collimated, "hot" jets where thermal pressure balances magnetic effects. The initial configuration is general and valid for all sub-Eddington nonrelativistic disks (modifications might occur in the very close vicinity of a black hole $R < 10R_S$) since it is assuming a Keplerian accretion disk in a vertical hydrostatic equilibrium and threaded by a bipolar magnetic field. This result differs from our previous study (CK02) by the inclusion of a realistic energy equation replacing the simplifying polytropic relation. The obtained jet displays a temperature higher than the disk one and is consistent with the creation of a hot corona. In this jet, we have shown that a significant part (~10%) of the jet power is enthalpy driven, and the thermal pressure is of the order of the magnetic pressure. Moreover, the present simulations started from an initial magnetic configuration with bent magnetic field lines and therefore prove unambiguously that the obtained collimation of the jet is self-consistently built up. We have, in addition, completely quantified the action of the magnetocentrifugal acceleration of matter, by demonstrating the force balance along field lines, as well as radially, showing the butterfly current circuit and fully diagnosing the energy transfer.

2. Evaluating energy fluxes through inner and outer radius, as well as through the disk surface, we presented the entire energy budget of the accretion-ejection structure. Unlike ADAF-like flows, we show that the main energy transport is achieved by the
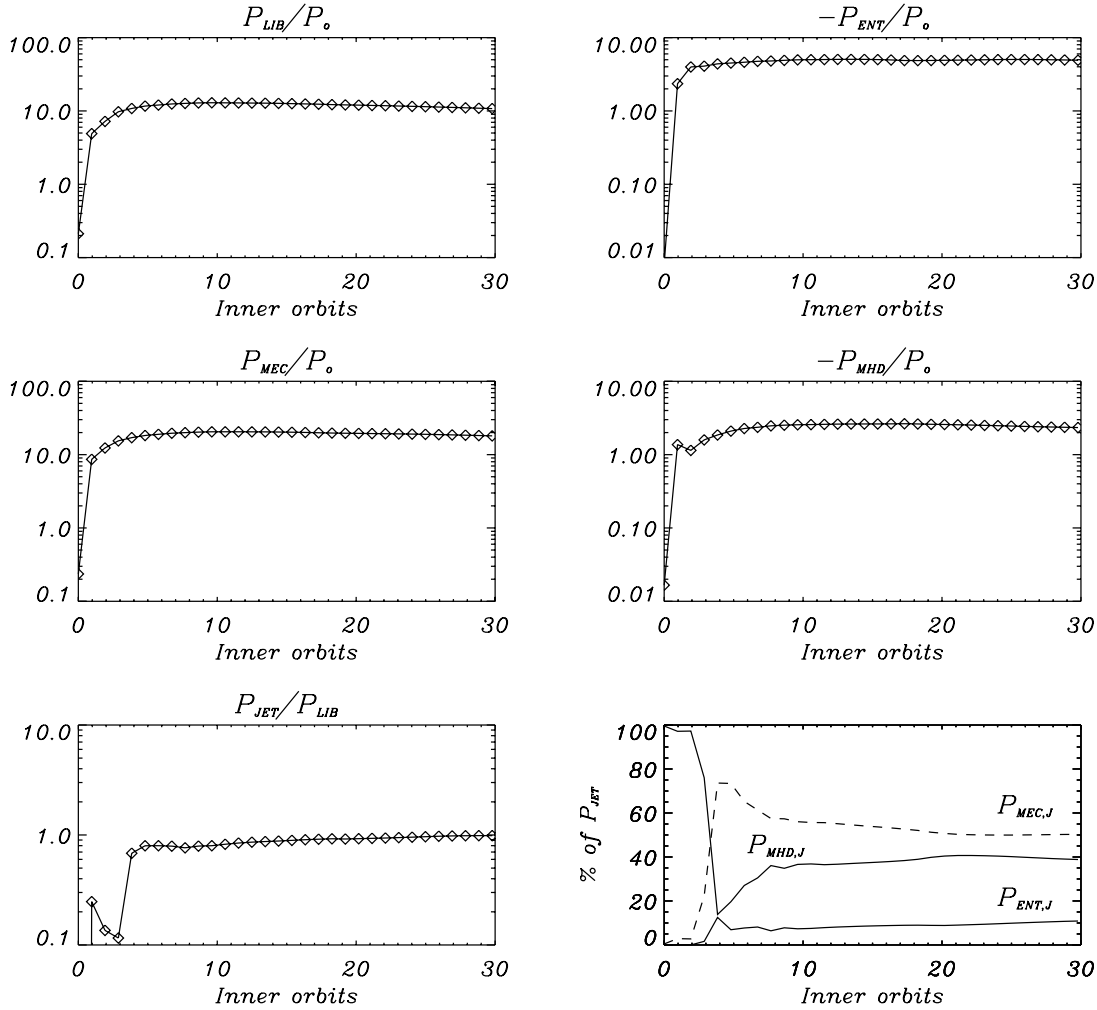
Fig. 9.—Temporal evolution of powers defining the complete energy budget as presented in § 4. The accretion-liberated power is nonvanishing in our structure, unlike ADAF-type flow. Indeed, disk enthalpy and magnetic energy fluxes are small compared to mechanical power, which is mainly sent into the jet. This structure is completely consistent with an underluminous disk launching bright jets.

jet that channels the major part of the energy released by accretion. This kind of flow can lead to underluminous accretion disks supporting bright jets (where the assumption of non-radiative plasma can no longer be valid), as, for instance, M87 (Di Matteo et al. 2003). In our simulations, the luminosity of the jet can be up to the energy liberated by the accretion $P_{\mathrm{JET}} \sim GM_* \dot{M}_A / 2R_I$, where $M_*$ is the mass of the central object and $R_I$ is the inner radius of the jet. Therefore, these simulations are a complete model of the generic "advection-dominated inflow-outflow solutions" (ADIOS) postulated by Blandford & Begelman (1999), where the authors suggested that outflows might carry a part of the total disk energy. The accretion disk with its associated hot jet is no longer subject to strong enthalpy creation as in ADAF. This also implies that this kind of accretion disk can remain thin, even if some local heating (like the ohmic heating included in the simulation) is occurring inside. Finally, these simulations adequately apply to both YSO- and AGN-type systems.

Forthcoming work will need to deal with alleviating the few simplifying assumptions in this work, the most prominent being the assumption of axisymmetry. This precludes our simulations from effects due to nonaxisymmetric instabilities that might perturb the flow (Kim & Ostriker 2000) or the equipartition disk

(Keppens, Casse, & Goedbloed 2002). We will be able to check the stability of our simulations by stepping into a three-dimensional framework. Another simplifying assumption was to suppose that the viscous torque is very small compared to the magnetic torque (as well as viscous heating small compared to Joule heating). The inclusion of viscosity in our simulations can lead to different kinds of flow where enthalpy creation can be enhanced and the jet luminosity correspondingly decreased. The transfer of angular momentum will then be more complicated (both radial by viscosity and vertical by the jet) but will undoubtedly enrich momentum, angular momentum, and energy transport phenomena within the accretion disk–jet system.

## REFERENCES

Blandford, R. D., & Begelman, M. C. 1999, MNRAS, 303, L1
Blandford, R. D., & Payne, D. G. 1982, MNRAS, 199, 883
Brackbill, J. U., & Barnes, D. C. 1980, J. Comput. Phys., 35, 426
Casse, F., & Ferreira, J. 2000, A&A, 353, 1115
Casse, F., & Keppens, R. 2002, ApJ, 581, 988 (CK02)
Di Matteo, T., Allen, S. W., Fabian, A. C., Wilson, A. S., & Young, A. J. 2003, ApJ, 582, 133
Di Matteo, T., Quataert, E., Allen, S. W., Narayan, R., & Fabian, A. C. 2000, MNRAS, 311, 507
Ferreira, J. 1997, A&A, 319, 340
Ferriera, J., & Pelletier, G. 1995, A&A, 295, 807
Hartigan, P., Edwards, S., & Ghandour, L. 1995, ApJ, 452, 736
Heyvaerts, J., & Norman, C. 1989, ApJ, 347, 1055
Igumenshchev, I. V., Narayan, R., & Abramowicz, M. A. 2003, ApJ, 592, 1042
Kato, S., Kudoh, T., & Shibata, K. 2002, ApJ, 565, 1035
Keppens, R., Casse, F., & Goedbloed, J. P. 2002, ApJ, 569, L121
Kim, W. T., & Ostriker, E. C. 2000, ApJ, 540, 372
Krasnopolski, R., Li, Z. Y., & Blandford, R. D. 1999, ApJ, 526, 631
Lery, T., Henricksen, R. N., & Fiege, J. D. 1999, A&A, 350, 254
Li, Z. Y. 1996, ApJ, 465, 855
Livio, M. 1997, in IAU Colloq. 163, Accretion Phenomena and Related Outflows, ed. D. T. Wickramasinghe, G. V. Bicknell, & L. Ferrario (ASP Conf. Ser. 121; San Francisco: ASP), 845
Lynden-Bell, D., & Pringle, J. E. 1974, MNRAS, 168, 603
Matsumoto, R., Uchida, Y., Hirose, S., Shibata, K., Hayashi, M. R., Ferrari, A., Bodo, G., & Norman, C. 1996, ApJ, 461, 115

Mirabel, I. F., Dhawan, V., Chaty, S., Rodriguez, L. F., Marti, J., Robinson, C. R., Swank, J., & Geballe, T. 1998, A&A, 330, L9
Mouschovias, T. C. 1976, ApJ, 206, 753
Narayan, R., & Yi, I. 1995, ApJ, 452, 710
Novikov , I. D., & Thorne, K. S. 1973, in Black Holes, ed. C. Dewitt & B. Dewitt (New York: Gordon & Breach), 343
Ouyed, R., & Pudritz, R. 1997, ApJ, 482, 712
Paczynsky, B., & Wiita, P. J. 1980, A&A, 88, 23
Rees, M. J., Begelman, M. C., Blandford, R. D., & Phinney, E. S. 1982, Nature, 295, 17
Rutten, R. G. M., Van Paradijs, J., & Tinbergen, J. 1992, A&A, 260, 213
Sauty, C., Trussoni, E., & Tsinganos, K. 2002, A&A, 389, 1068
Serjeant, S., Rawlings, S., Lacy, M., Maddox, S. J., Baker, J. C., Clements, D., & Lilje, P. B. 1998, MNRAS, 294, 494
Shakura, N. I., & Sunyaev, R. A. 1973, A&A, 24, 337
Shapiro, S. L., Lightman, A. P., & Eardley, D. M. 1976, ApJ, 204, 187
Tóth, G. 1996, Astrophys. Lett. Commun., 34, 245
Tóth, G., & Odstrčil, D. 1996, J. Comput. Phys., 128, 82
Ushida, Y., & Shibata, K. 1985, PASJ, 37, 515
Ustyugova, G. V., Koldoba, A. V., Romanova, M. N., Chetchetkin, V. M., & Lovelace, R. V. E. 1995, ApJ, 439, L39
———. 1999, ApJ, 516, 221
von Rekowski, B. V., Branderburg, A., Dobler, W., & Shukurov, A. 2003, A&A, 398, 825
Wardle, M., & Königl, A. 1993, ApJ, 410, 218